

Journal of Geophysical Research: Planets

RESEARCH ARTICLE

10.1002/2014JE004774

Key Points:

- Crustal magnetic field implies substantial intrusive volumes beneath Syrtis Major
- Free-air gravity anomaly data imply mafic residue beneath edifice following crystal fractionation
- The intrusion zone is elongated north-south by structures tangential to Isidis Basin

Correspondence to:

R. J. Lillis,
rlillis@ssl.Berkeley.edu

Citation:

Lillis, R. J., J. Dufek, W. S. Kiefer, B. A. Black, M. Manga, J. A. Richardson, and J. E. Bleacher (2015), The Syrtis Major volcano, Mars: A multidisciplinary approach to interpreting its magmatic evolution and structural development, *J. Geophys. Res. Planets*, 120, doi:10.1002/2014JE004774.

Received 12 DEC 2014

Accepted 27 JUL 2015

Accepted article online 31 JUL 2015

The Syrtis Major volcano, Mars: A multidisciplinary approach to interpreting its magmatic evolution and structural development

Robert J. Lillis¹, Josef Dufek², Walter S. Kiefer³, Benjamin A. Black⁴, Michael Manga⁴, Jacob A. Richardson⁵, and Jacob E. Bleacher⁶

¹Space Sciences Laboratory, UC Berkeley, Berkeley, California, USA, ²Georgia Tech Department of Earth and Space Sciences, Atlanta, Georgia, USA, ³Lunar and Planetary Institute, Houston, Texas, USA, ⁴Department of Earth and Planetary Sciences, UC Berkeley, Berkeley, California, USA, ⁵School of Geosciences, University of South Florida, Tampa, Florida, USA, ⁶NASA Goddard Space Flight Center, Greenbelt, Maryland, USA

Abstract Very weak crustal magnetic fields over the Syrtis Major volcanic complex imply almost total thermal demagnetization via magmatic intrusions over a large area less than ~4 Ga. We fit a model of these intrusions and the resulting thermal demagnetization to maps of crustal magnetic field strength at 185 km altitude. The best fits are most consistent with a “dog bone”-shaped region of intrusive material, elongated approximately north-south, with an area of ~350,000 km² and an inferred volume of ~4–19 × 10⁶ km³. Such a large volume is best explained by a long-lived mantle plume beneath the Syrtis edifice. A free-air gravity anomaly high over the Syrtis Major caldera is consistent with dense mafic residue remaining at depth following crystal fractionation that produced the silicic magmas seen at the surface. The elongation of this region is consistent with ascent and north-south emplacement of magma enabled by structures parallel to and associated with the preexisting Isidis impact basin.

1. Introduction

Magmatic activity on Mars, just as on Earth, alters the magnetic properties of the planet’s crust. If a substantial volume of crust is magnetically altered, the magnetic field signature of the alteration should be resolvable even from orbital altitudes. As magnetic minerals are heated above their Curie temperatures (T_{Curie}), any prior magnetization is erased. As the crust cools again, its magnetic minerals acquire a new magnetization proportional to the strength of the ambient magnetic field and to their magnetic susceptibility as they cool through their Curie temperatures [Pauthenet and Bochirol, 1951; Schmidt and Clark, 1985].

Although some magnetized crust (up to 40 km) beneath crater-dated lava flows has led to interpretations that the Martian dynamo continued until ~3.7 Ga [e.g., Lillis *et al.*, 2006; Milbury and Schubert, 2010; Milbury *et al.*, 2012], magnetic and crater retention age analysis of large-impact craters >300 km in diameter (which, unlike surface lava flows, reset the magnetization over the full depth of crust) implies that Mars has not hosted a global magnetic field since ~4 Ga [Arkani-Hamed, 2004; Lillis *et al.*, 2008a, 2013a]. Regardless, Martian crust that has been demagnetized by magmatic intrusion in the last ~4 Ga cannot have subsequently acquired, upon cooling, any substantial thermoremanent magnetization (TRM). It follows then that magmatic activity younger than ~4 Ga in previously magnetized areas, if significant enough to cause thermal demagnetization on length scales larger than the measurement altitude, will result in reduced measured magnetic field amplitudes. Considering this and if other mechanisms of demagnetization can be excluded, areas of low or undetectable magnetic field in volcanic settings can be associated with magmatic intrusions without the terrestrial complications of induced magnetization, subsequent TRM, or subtracting the magnetic fields of a core dynamo, all of which apply on Earth. Mars thus offers a rare opportunity to map the location and volume of intruded bodies of magma beneath volcanic edifices through the signature of thermal demagnetization in the magnetic field. Unlike gravity studies, this method does not require that density differences between intrusion and country rock can be estimated *a priori*.

The phenomenon of large-scale thermal demagnetization is most readily apparent in the Tharsis volcanic province. Tharsis is an enormous, high-standing region containing several large and many small shield volcanoes that dominate the western hemisphere of Mars, covering ~20–25% of the planet’s surface [e.g.,

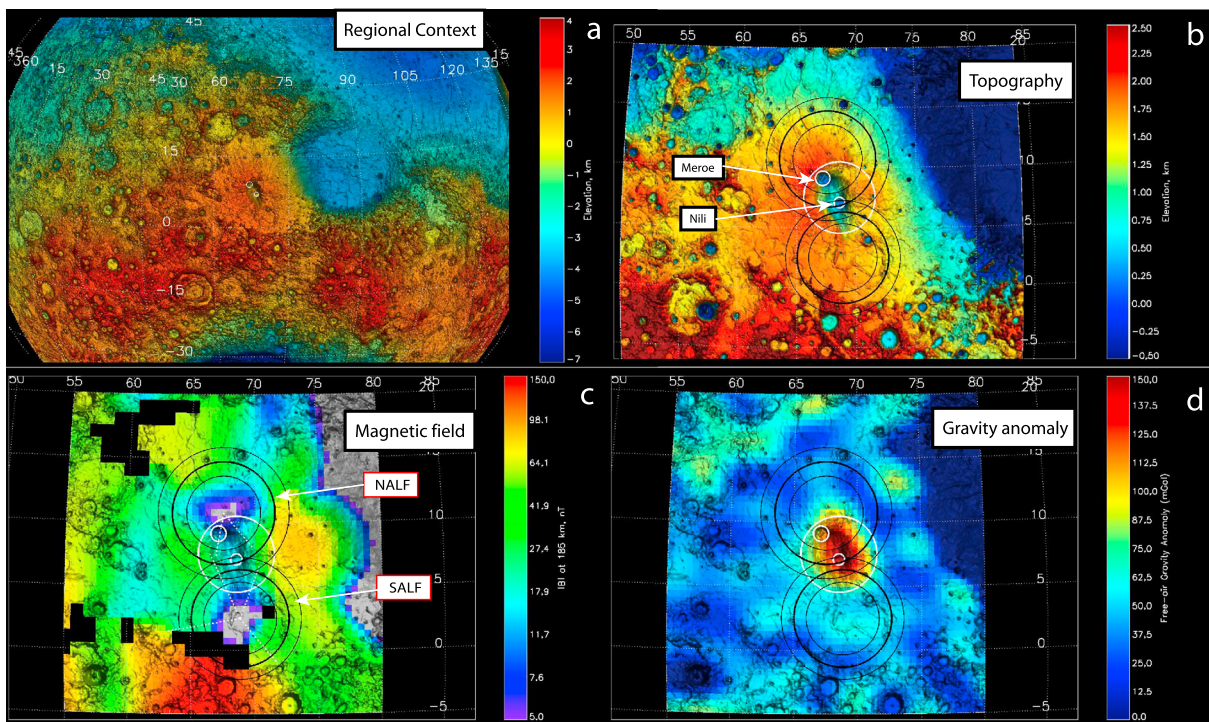


Figure 1. (a) The regional context of the Syrtis Major volcanic province showing its position just west of the Isidis Basin and that it is substantially younger than the ancient highland crust to its north, west, and south. Orthographic maps of (b) surface topography derived from MOLA data, (c) magnetic field magnitude at an altitude of 185 km, and (d) free-air gravity anomaly data for the Syrtis Major region. The small white circles in Figures 1a and 1b are the calderas of Meroe (north) and Nili (south) Paterae. The larger white circle represents a high-density cylindrical intrusive body modeled to fit the gravity anomaly data (see Figure 2). The northern and southern areas of low magnetic field (NALF and SALF) are labeled in Figure 1b. The large black circles represent the cylindrical areas of magmatic intrusion (with 1 sigma uncertainties as thinner circles) modeled in this paper to fit the magnetic field data, i.e., with radii shown in the yellow boxes of Table 3: 234 ± 66 km and 225 ± 57 km for the NALF and SALF zones, respectively.

Carr, 1974]. Considering the planet as a whole, Tharsis' crust is both the thickest (~90 km [Konopliv et al., 2011; Neumann et al., 2004]) and has the weakest magnetic field signature as measured from orbit, with an upper bound of just 0.8 nT at 185 km altitude. In contrast, the margins of Tharsis host moderate-to-strong crustal magnetic fields (up to hundreds of nanotesla at 185 km). Given the $\sim 20 \times 10^6 \text{ km}^2$ of lava flows identified on the surface [Carr, 1974; Wise et al., 1979], the very weak magnetization of the Tharsis region is best explained by long-lived pervasive magmatism and thermal underplating, likely involving hundreds of millions of cubic kilometers of intruded magma [Dohm et al., 2009; Johnson and Phillips, 2005; Lillis et al., 2009].

Although there exist other volcanic regions of Mars devoid of detectable crustal magnetism (e.g., Elysium Mons, Amphitrites Patera, and Peneus Patera), Syrtis Major is the only other volcanic setting with a magnetic signature best explained by the intrusion of substantial amounts of magma into crust that was previously significantly magnetized [Lillis et al., 2008b]. In this paper, we update the magnetic and thermal modeling techniques described by Lillis et al. [2009], in combination with inferences from gravity data, to place constraints on the geographic extent and total volume of magma intrusions at the Syrtis Major volcano, west of the Isidis Basin near the highland-lowland dichotomy. We present evidence that magmatism at Syrtis was long lived. Our magnetic, thermal, and gravity data—in conjunction with estimates of volumes of erupted lavas—also allow us to infer the patterns of magma migration and the compositional evolution of magmas over the life of the volcano.

2. Data

Using pitch angle distributions of suprathermal electrons measured by the Mars Global Surveyor (MGS) Magnetometer/Electron Reflectometer (ER), Lillis et al. [2008b] produced a map of the field magnitude $|B|$, due to crustal sources only, at 185 km altitude above the Martian datum, hereafter referred to as B_{185} . This map has an approximate spatial resolution of ~ 200 km and a detection threshold for crustal fields of $\sim 1\text{--}4$ nT. Data gaps (shown in black in Figure 1a) exist where magnetic field lines are permanently closed,

i.e., where they are attached to the crust at both ends, forbidding reflection of solar wind electrons. This represents our primary data set for constraining magmatic intrusions in this study. For context, we also examine Mars Orbiter Laser Altimeter (MOLA) topography [Smith *et al.*, 2001] at a resolution of 0.03125° (1.85 km) per pixel, and the most recent publicly available Mars free-air gravity anomaly data set Jet Propulsion Laboratory (JPL) model JGMRO1110C expanded to degree and order 90 [Konopliv *et al.*, 2011].

3. The Syrtis Major Volcanic Construct: Geological and Geophysical Context

Frequently appearing as a large dark spot on the surface of Mars, Syrtis Major has the distinction of being the first surface feature ever documented on another planet (by Christiaan Huygens in 1656 [Schilling, 2011]).

3.1. Morphology

On the basis of spacecraft images and Earth-based radar data, it was identified as a low-relief volcanic construct by Schaber [1982]. It is approximately 1000 km in east-west dimension and 1400 km in north-south extent, and lies near the edge of the global dichotomy boundary, centered at 8°N, 67°E (Figure 1a). Its summit is ~2300 m above the Martian datum, and many of the shallow-sloped (i.e., 0.25°–0.5°) major flows on its flanks date approximately to the Hesperian epoch of Mars, around 3.5 Ga [Plescia, 2004; Tanaka, 1986]. Some flows overlie Nili Fossae to the northeast and breach the rim of the ~1200 km diameter Isidis impact basin to the east. From topographic profiles and spot estimates of lava thickness, the total volume of lava comprising the edifice has been estimated at $1.6\text{--}3.2 \times 10^5 \text{ km}^3$ [Hiesinger and Head, 2004]. MOLA topography of the region is shown in Figure 1b.

3.2. Caldera Topography and Eruptive History

The central portion of Syrtis is characterized by two named calderas, Meroe and Nili Paterae: ~70 km and ~50 km in diameter, 1.9 km and 1.6 km deep, and located to the north and south of the volcano, respectively. They sit in a 300 km × 150 km wide depression, elongated approximately NNE to SSW [Hiesinger and Head, 2004; Plescia, 2004], which may be an older caldera [Werner, 2009], indicating collapse into a vast, partially evacuated magma chamber [Hiesinger and Head, 2004]. Both Meroe and Nili calderas contain several overlapping subcalderas with different crater-count ages, indicating a long-lived source of magma and repetitive magma chamber inflation and discharge over the history of Mars. Meroe underwent its oldest resolvable extrusive episodes at 3.6–3.8 Ga, whereas its most recent episode was less than 1.4 Ga and possibly as recently as 230 Ma [Robbins *et al.*, 2011]. Where not obstructed by dark dune fields, the subcalderas within Nili Patera have ages between 1.6 Ga and 3.6 Ga [Robbins *et al.*, 2011]. Syrtis Major is clearly a long-lived volcanic system, with activity spanning a period of 2.2–3.6 Ga of Martian history.

3.3. Mineralogy and Composition of Syrtis Major

The only major volcanic construct on Mars not layered with obscuring dust, the surface composition of Syrtis Major, has been studied extensively with orbital remote sensing observations. Exposures on Syrtis have been inferred to indicate the presence of diverse magma types from komatiites to rhyolites and indicate prolonged magmatic evolution [e.g., Christensen *et al.*, 2005; Hamilton and Christensen, 2005; Hiesinger and Head, 2004; Mustard *et al.*, 2005; Wray *et al.*, 2013]. Hiesinger and Head [2004] gave a detailed summary of the wide variety of erupted igneous compositions inferred by many authors, ranging from andesites to komatiites. Rampey and Harvey [2012] suggested that during the late Hesperian, Syrtis lavas transitioned from ultramafic to primarily basaltic compositions. The earlier ultramafic lavas indicate a high degree of partial melting in the mantle. The subsurface of Syrtis (i.e., outcrops of the original Noachian crust or older lava flows covered by those on the surface, exposed by impacts and erosion) also shows signs of carbonate decomposition and magma-carbonate interaction, as inferred from thermal emission spectra [Glotch and Rogers, 2013]. The Nili Patera dacite, identified by Christensen *et al.* [2005], has been interpreted to be 3.0–3.6 Ga based on crater counts [Robbins *et al.*, 2011], and so likely postdates the main phase of Syrtis Major's formation [Hiesinger and Head, 2004]. Other highly felsic rocks, interpreted to be rhyolitic, appear even younger (i.e., 2–3 Ga), albeit with relatively poor age constraints [Wray *et al.*, 2013]. Here we use the volcanic rock types "dacite" and "rhyolite" to denote composition, but spectroscopic observations do not reveal whether the exposed lithologies are intrusive or extrusive. The multiple calderas, wide range of ages, and presence of silicic magmas imply a prolonged history of magmatism at Syrtis. Fractional crystallization in a magmatic mush at shallow crustal levels can account for the range of compositions observed at Nili [Wray *et al.*, 2013]. Such a scenario implies that a denser, more mafic residue remains at depth.

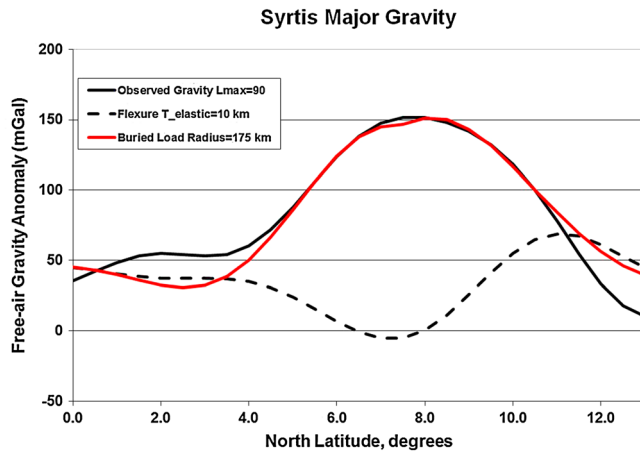


Figure 2. The Syrtis Major gravity anomaly (black solid line) is best fit by a model (red line) that includes both flexurally supported topography (dashed black line) and a dense subsurface load.

3.4. Gravity Evidence for a Dense Buried Load

While the presence of a magma chamber beneath Syrtis can be inferred from the presence of the calderas, gravity data have been used to characterize its possible areal extent ($\sim 700 \times 350$ km) and thickness (several kilometers) [Kiefer, 2004]. The large positive gravity anomaly measured over the Syrtis caldera complex (see Figure 1c) requires either a large upward deflection of the crust-mantle boundary or a solidified magma chamber at least partially filled with dense igneous cumulates (olivine or pyroxene). Although we argue later (section 5.7) that a mantle plume was probably responsible for creating the Syrtis Major volcanism, the bulk of the observed volcanism has cratering ages that exceed 2–3 Ga [Hiesinger and Head, 2004]. Over that long time interval, any dynamic uplift of the crust that might have been originally produced by the plume would have decayed. Because of this, and because of the large volumes of volcanic material identified at Syrtis, we regard a solidified magma chamber as the more geologically reasonable mechanism for producing the gravity anomaly.

Here we reexamine the Syrtis Major gravity anomaly using the gravity model of Konopliv *et al.* [2011], which is based on Doppler tracking data from the Mars Reconnaissance Orbiter (MRO), as shown in Figure 2. All profiles are taken along 69°E. The free-air gravity model in the solid black line (in Figure 2) is JPL model JGMRO110C, expanded to spherical harmonic degree 90 (to which we applied a cosine taper at $L = 85\text{--}90$), implying a block size (half-wavelength resolution) of ~ 120 km. The dashed black line is the free-air gravity anomaly due to topography supported by a 10 km thick elastic lithosphere, with Young's modulus of 10^{11} Pa, Poisson's ratio of 0.25, and a density difference between crust and mantle of 700 kg m^{-3} . As noted by Kiefer [2004], the substantial mismatch between the observed free-air gravity anomaly and the gravity from topography indicates the need for an additional contributing mass. The red line in Figure 2 is a gravity model that includes both the flexurally supported topography and a dense subsurface load, which is modeled as a finite thickness spherical cap following the method of Kiefer [2004] and Kiefer [2013]. The load is 175 km in radius; is centered at 7.5°N, 68.75°E; and is 4.7 km thick based on a density contrast of 600 kg m^{-3} between the intrusion and the crust, which is assumed to be moderately porous basalt.

This gravity signature may correspond to dense mafic cumulates that settled in the magma chamber. Measured grain densities for Martian nakhelite and chassignite meteorites (pyroxene- and olivine-dominated cumulates, respectively) range from 3400 to 3700 kg m^{-3} [Macke *et al.*, 2011]. Alternatively, the density contrast indicated by the gravity data may be due to thermal annealing of pores in the crust (which were present prior to volcanic activity and that annealed after new dikes and sills intruded beneath the caldera), as postulated for the lunar Marius Hills [Kiefer, 2013]. In either case, the density anomaly is almost certainly related to magmatic activity and so indicates that thermal demagnetization may have been substantial. Under a scenario where the density contrast is from porosity annealing, the subsurface layer could be 10–20 km thick in the center of the load; conversely, a layer thickness of about 5 km is required for a pyroxene-dominated cumulate layer and about 3 km for an olivine-dominated cumulate layer. If the gravity anomaly is due to a pyroxene-dominated cumulate

composition, the inferred volume of the magma chamber is $3.5 \times 10^5 \text{ km}^3$, which is similar to the total exposed volume of the Syrtis major shield [Hiesinger and Head, 2004]. However, the magma chamber observed in the gravity data is likely to be just a small fraction of the total subsurface (intrusive) volume of the volcanic complex (see section 5.6). If composition is olivine dominated, the inferred volume is ~40% less or $\sim 2 \times 10^5 \text{ km}^3$. Due to the limited topographic relief of the volcanic shield, much of the inferred volume of the cumulate chamber must occur within the basement beneath the volcano, rather than within the shield itself. Although the spatial resolution of the gravity field used in this study is almost twice that of the gravity field used by Kiefer [2004], the inferred horizontal extent and vertical thickness of the cumulate chamber is similar in the two studies.

The modeled positive density anomaly magma chamber (whether due to a dense cumulate layer or thermally annealed porosity) only contributes to the gravity anomaly between 4 and 11°N; beyond these bounds, the model gravity is essentially entirely due to the flexurally supported topography, as shown by the overlap of the dashed black and solid red lines in Figure 2. There are small misfits between the observed and model gravity anomalies between 1° and 4°N and between 12° and 14°N, with typical misfits of 15–30 mGal. The observed gravity field has a likely uncertainty of about 10 mGal [Konopliv et al., 2011], so it is likely that these misfits are real but the details of the misfits are probably not well determined. Between 1° and 4°N, the gravity due to topography is less than the observed free-air gravity, suggesting the presence of a thin layer of dense subsurface material, possibly a southward extension of the magma chamber system. Between 12° and 14°N, the gravity due to topography exceeds the observed free-air anomaly, indicating the presence of a low-density subsurface structure. Preliminary modeling suggests that both the structures responsible for the southern and northern misfits are likely to be thin (<1–2 km, depending on the density contrast). However, because these structures are close to the uncertainty level in the observed gravity field, we have not attempted detailed modeling of these features.

3.5. Magnetic Field Evidence for Magmatic Intrusions

Geophysical potential theory [e.g., Blakely, 1995] holds that regions above which near-zero magnetic fields are measured must have near-constant magnetization in the magnetizable layer of crust near the surface. However, in the case of volcanic settings on Mars where the magnetization was acquired $>\sim 4$ Ga ago, the magnetization in such regions is almost certain to be near zero. There are three primary reasons for this: (a) natural mineralogical variation leads to variability in the magnetic susceptibility of the rocks holding the TRM, leading to inhomogeneous magnetization strength; (b) natural variability in the thickness of the cooling lava or magma; and (c) shock and thermal demagnetization from subsequent impacts would cause inhomogeneities in any putative uniformly magnetized layer. Note that (a) and (c) also mean that low magnetic field measured within large-impact craters also points strongly to near-zero magnetization.

Apart from obvious impact demagnetization in the Isidis Basin to the east [Lillis et al., 2010], the surrounding $\sim 10 \times 10^6 \text{ km}^2$ around Syrtis contains mostly moderate-to-strong crustal magnetic fields, averaging $\sim 40 \text{ nT}$ but rising to as much as 200 nT (see Figure 1a). However, as noted by Lillis et al. [2008b], a “tilted hourglass”-shaped zone of low magnetic field strength exists over the central part of Syrtis. In particular, two distinct areas of very low field strength (<5 nT) exist at 10.7°N, 67.7°E and 2.5°N, 68.5°E. When taken with the other geological and geophysical data sets mentioned thus far, these areas of low field strength strongly suggest thermal demagnetization by volcanic intrusions. We denote these two regions as south and north areas of low field magnitude (SALF and NALF, respectively).

While the ER data set has the kind of dense coverage that is well suited to this kind of study, the MGS magnetometer [Acuña et al., 1999] took data during two low-altitude passes approximately north-south over Syrtis Major, one of which was largely free of noise from ionospheric currents and is at an altitude of 113–122 km over the volcanic edifice. This pass (not shown) has minima of $\sim 20 \text{ nT}$ at 2.5°N and 9.5°N latitude and a maximum of 70 nT at 7°N latitude, matching very well the morphology shown in Figure 1 and supporting the ER data set.

4. Methods: Fitting Statistical Models of Thermal Demagnetization

We calculated azimuthally averaged magnetic field profiles at an altitude of 185 km resulting from a range of plausible three-dimensional postintrusion magnetizations for both the NALF and SALF locales, as discussed below. We then compared these calculated profiles with the corresponding measured profiles of B_{185} , to estimate the areal extent and total volume of the intrusions at each site.

4.1. Monte Carlo Magnetization Model

We used the statistical Fourier domain technique of *Lillis et al.* [2010] to stochastically model crustal magnetization and the thermal demagnetization thereof and then to calculate the resulting magnetic fields that would be observed at orbital altitudes. We use this instead of standard magnetic inversion techniques for two main reasons: (1) such inversions with scalar magnetic data require many assumptions and do not easily converge and (2) we are interested only in azimuthal averages, not exact fits of the two-dimensional field as would be required by a standard magnetic inversion technique. In other words, our technique is more appropriate to the problem at hand.

In this study, we created random magnetization patterns with all 225 combinations of the following characteristics:

1. Magnetization strength was distributed according to a Gaussian distribution with full width at half maximum (FWHM) ranging logarithmically from 0.5 to 500 A/m in 75 steps. Positive and negative magnetizations in this case simply mean parallel or antiparallel to a single magnetization axis chosen at 45° to the horizontal (such a choice results in an error of less than 15% compared to other directions [*Lillis et al.*, 2010]).
2. A single Gaussian distribution of vertical magnetization coherence wavelengths centered on 12 km with a full width at half maximum (FWHM) of 2.5 km. This value is in some ways unimportant since normalized magnetic field profiles are independent of vertical coherence scale [*Lillis et al.*, 2010, section 3.3.3].
3. A single total preintrusion magnetic layer thickness of 40 km, consistent with published global estimates [*Dunlop and Arkani-Hamed*, 2005; *Voorhies*, 2008].
4. Gaussian distributions of horizontal coherence wavelengths centered on 256 km, 512 km, and 1024 km, with FWHMs equal to 20% of the central value. The last value has been shown to be close to the global average value [*Voorhies*, 2008; *Lillis et al.*, 2010, cf. Figure 5]. However, given that the extent of the magnetized region between the low magnetic field zones of Syrtis and the demagnetized Utopia and Isidis Basins may be as little as hundreds of kilometers, examining smaller coherence wavelengths is appropriate.

At our observation altitude of 185 km, the magnetic field magnitude depends linearly on magnetization strength, vertical coherence wavelength, and total layer thickness (the first three variables described above). As we are not trying to determine these three parameters separately, we only varied the magnetization strength [*Lillis et al.*, 2010] to compute a representative series of magnetization patterns. We note here that random magnetization patterns with these properties (an example of which is shown in three dimensions in Figure 2 of *Lillis et al.* [2010]) are consistent with orbital data and are qualitatively realistic in the sense that 12 km and 256 km, 512 km, and 1024 km are quite plausible average values for approximately twice the size of a coherently magnetized piece of Martian crust in the vertical and horizontal directions, respectively.

4.2. Magma Intrusion Modeling

We used thermal modeling of magmatic intrusions to assess the peak temperature conditions achieved in the crust. We focused on characterizing the sensitivity of the thermal state of the crust in response to both the radial extent of intrusions emplaced from a central axis and to different magma fluxes. We use a three-dimensional axisymmetric model of intrusion because, as mentioned in the previous section, we are interested only in azimuthal averages of magnetization and magnetic field. In our simulation domain with a radius of 1000 km and depth of 40 km, we modeled magmatic intrusions stochastically as dikes and sills of 200–800 m thickness and with an average lateral extent of 70 km. These dimensions are consistent with large igneous provinces on Earth [*Elliot et al.*, 1999]. We used a finite volume modeling approach [*Dufek and Bergantz*, 2005] to examine conductive heat transfer in the crust. We included nonlinear relationships between melt fraction and temperature based on petrologic experiments [*Green*, 1972, 1982; *Green and Ringwood*, 1968; *Petcovic and Dufek*, 2005].

Prior to the intrusion of magma, the crust was assumed to have had a thermal gradient of 16 K/km, which is appropriate for the Noachian/Hesperian time frame in which most Syrtis Major volcanism occurred [*Hauck and Phillips*, 2002; *Morschhauser et al.*, 2011; *Williams and Nimmo*, 2004]. The magma in our models was intruded at its liquidus temperature, and the thermal properties of the intruded magmas and crust are identical to those presented by *Lillis et al.* [2009]. To examine the effect of changes in the spatial extent of the magmatic province, we conducted simulations in which the intrusions were confined to a specific radial distance of the axis of the simulations. This distance was varied between 100 km and 400 km from the axis in seven linear steps (i.e., 100 km, 150 km, and 200 km). For each radial constraint, five different intrusion flux scenarios were considered, with the ratio of intruded magma volume to preexisting crustal volume at the end of the modeled intrusive

episode was 7×10^{-4} , 4×10^{-3} , 2×10^{-2} , 1×10^{-1} , and 5×10^{-1} . Magma intrusion was simulated over a 100 Ma time frame, but the entire simulation was run for 500 Ma in order to examine far-field heating of the crust, away from the active intrusions. For the 100 Ma duration of intrusion, the thermal effects of each intrusion were largely independent, and so we therefore refer to the ratio of total intruded volume of intrusive magma to pre-existing crust. The maximum temperature (which is recorded) is the peak temperature at each location from the start of an intrusive episode (which includes many distinctive dike and sill intrusions) until all intrusions have ceased and the crust has cooled following the waning of intrusions.

Intruding a given magmatic volume over a longer time frame than 100 Ma had only a minor impact on the maximum temperature recorded in the spatial domain (shown in Figure 4a). The majority of intrusions in our model were idealized as sills and were accommodated by displacing underlying crust downward, thus leading to crustal thickening. In these simulations we only considered magma volume accommodation by crustal thickening rather than by lateral extension, although our previous work has shown no substantial difference in the total intrusion volume required to fit the magnetic field data [Lillis *et al.*, 2009]. Assumptions for physical parameters are identical to those reported in section 4.1 of Lillis *et al.* [2009], which also includes a detailed description of our magma intrusion model.

4.3. Modeling of Thermal Demagnetization

As magnetic minerals increase in temperature, TRM decreases slowly and quasilinearly at first, then more rapidly as T_{Curie} (the temperature at which magnetization drops to zero) is approached. We chose to represent experimental curves for thermal demagnetization of TRM empirically, using a modified version of the cumulative distribution function of the gamma distribution:

$$|M| = \begin{cases} \frac{\gamma\left(\beta, \frac{T_{\text{Curie}} - T}{T_{\text{scale}}}\right)}{\Gamma(\beta)}, & T < T_{\text{blocking}} \\ 0, & T \geq T_{\text{blocking}} \end{cases}, \quad (1)$$

where T is the temperature in kelvin, $|M|$ is the normalized remaining magnetic moment, Γ is the gamma function, γ is the lower incomplete gamma function, β is a shape parameter, T_{scale} is a scale parameter, and T_{Curie} is the Curie temperature at which a mineral becomes paramagnetic and loses all of its TRM; i.e., its magnetization drops to zero. We found that thermal demagnetization data for pyrrhotite ($T_{\text{Curie}} = 325^\circ\text{C}$) [Dekkers, 1989], magnetite ($T_{\text{Curie}} = 580^\circ\text{C}$) [Dunlop, 2009], and hematite ($T_{\text{Curie}} = 670^\circ\text{C}$) [Ozdemir, 2005] could be fit reasonably accurately by equation (1), as shown in Figure 3. Table 1 shows the best fit values for β and T_{scale} . The best fits match the experimental curves for magnetite and pyrrhotite quite well. The fit for hematite is not as close, but, given the final uncertainties in inferred magma intrusion radii (~25%) and volumes (~60%), these fits are adequate for our purposes.

We note a caveat that the precise shape of the demagnetization curve depends on the history of cooling when the rock first acquired its TRM, as well as the mineral grains present [e.g., Dunlop, 2009], and so the data shown in Figure 3 do not necessarily apply to all possible instances of these minerals on Mars.

Figure 4 demonstrates how this demagnetization parameterization is applied in our model. Figure 4a is an example of a cross section of the 3-D cylindrically symmetric array of maximum temperature reached during intrusion simulation. Figure 4b shows the resulting fraction of the original magnetization remaining after thermal demagnetization has been applied according to equation (1) and the fitting parameters in Table 1. Figure 4c shows the same data as Figure 4b but resampled to the spatial resolution of the magnetic simulation. It can be thought of as a “mask” which we place over the preintrusion 3-D magnetization patterns, resulting in a postintrusion magnetization pattern like the example in Figure 4d. Figure 4e shows the azimuthally averaged radial profiles of B_{185} calculated when this mask is applied to 100 randomly chosen patterns (as well as the average of those patterns).

For this study, we performed this calculation for 200 randomly chosen patterns (to achieve statistical robustness) for each combination of the parameters shown in Table 2, for a total of 4,725,000 forward models.

4.4. Fitting to Measured Profiles of B_{185}

We calculated azimuthally averaged profiles of the mean and standard deviation of B_{185} for both the SALF and NALF from the ER data. We excluded the small “slice” of each in the weak-field region where the circles

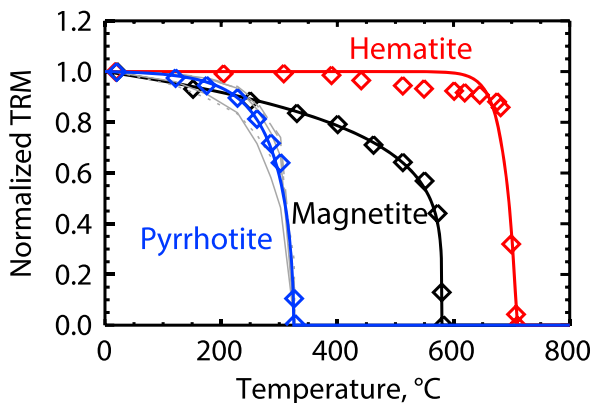


Figure 3. Measured and fitted thermal demagnetization curves. Experimental data of thermal removal of TRM (thermoremanent magnetization) are shown with black diamonds for a $110\text{ }\mu\text{m}$ sample of magnetite [Dunlop, 2009], blue diamonds and light gray lines for the average and standard deviations of a representative number of samples of pyrrhotite [Dekkers, 1989], and red diamonds for a $10 \times 6 \times 2\text{ mm}$ hematite crystal [Özdemir, 2005]. The solid lines represent the best fits to these data using the formula in equation (1). Best fit parameters are shown in Table 1.

radial bin divided by the square root of the number of data points in that bin. This resulted in a five dimensional χ^2 space, where the dimensions are as follows: magnetization coherence wavelength, magnetization strength, magma intrusion rate, magma intrusion radius, and Curie temperature.

We considered all points in this space within the 1 sigma error ellipsoid [e.g., Bevington and Robinson, 2003] to be acceptable fits. The validity of this approach rests upon the assumption of an approximately normal distribution of residual values, which was found to be the case for magnetization strength and intrusion radius, but could not be conclusively shown for Curie temperature, coherence wavelength, or magma intrusion rate due to the small number of values in those dimensions (see Table 2). However, Lillis et al. [2010] used the same modeling framework and data set to study demagnetization by meteorite impact and found approximately normally distributed residuals for the dimensions of coherence wavelength, magnetization strength, demagnetization radius, and a parameter analogous to Curie temperature for pressure demagnetization.

Figure 5 shows the B_{185} data and the family of acceptable model curves (i.e., within the 1 sigma error ellipsoid), as well as the distribution of best fits in terms of intrusion radius and volume. Figure 6 shows the means and standard deviations of intrusion radius and total intrusion volume corresponding to these acceptable fits for each of the three magnetic minerals and coherence wavelengths. These values are also given in Table 3.

Note that we do not show the fitting results for magnetization strength, for two reasons: the first is that magnetic field has a linear dependence on magnetization strength and therefore is completely separable from the other fitting parameters; i.e., knowledge of the absolute magnetization strength is not required to constrain Curie temperatures, lateral magnetization coherence wavelengths, or intrusion radii or volumes. The second reason is that magnetic field also has a linear dependence on the vertical coherence wavelength of the magnetization, rendering any fitting results valid only for the assumed vertical magnetization coherence wavelength of 12 km, a value that is not unreasonable but nonetheless cannot be constrained.

5. Results and Discussion

The inherently nonunique relationship between magnetic field and magnetization means that similar radial profiles of B_{185} can result from a range of possible thermal demagnetization scenarios. There is thus a

Table 1. Parameters Describing Fits of Equation (1) to Thermal Demagnetization Data for the Three Minerals Considered in This Study

Mineral	T_{Curie}	β Shape Parameter	T_{scale}	Scale Parameter
Pyrrhotite	325°C	0.21	5316	
Magnetite	580°C	0.35	152.3	
Hematite	670°C	1.06	20.63	

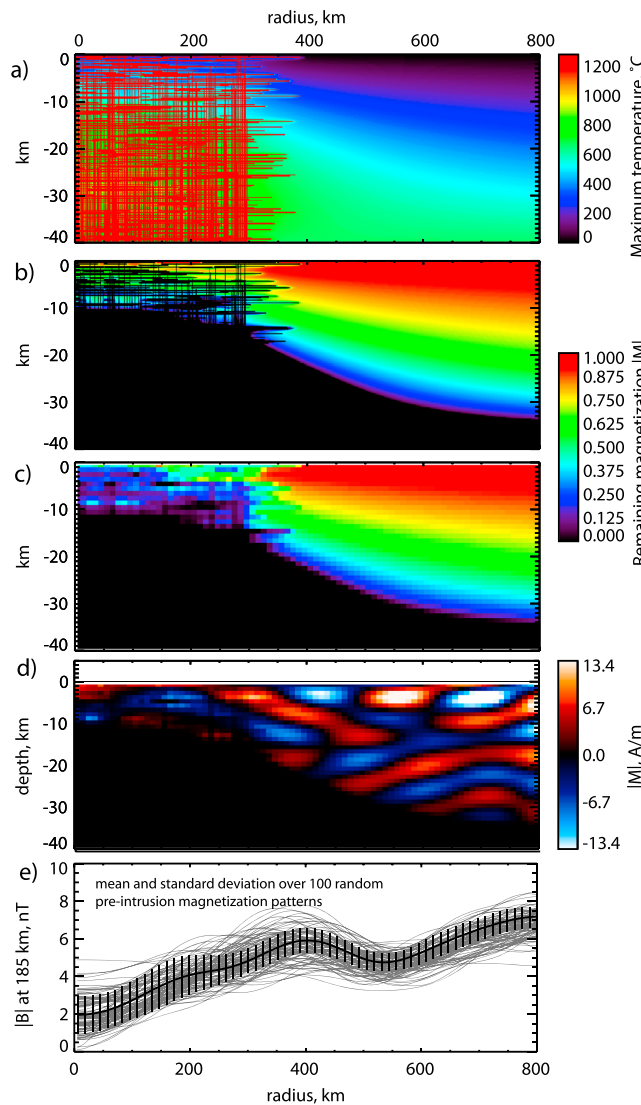


Figure 4. An illustration of the thermal demagnetization model. (a) The maximum temperature reached in the magma simulation domain as a function of depth. (b) The fractional magnetization remaining after the intrusions and 100 Ma of subsequent thermal conduction (assuming that the magnetic carrier is magnetite) at the spatial resolution of the magma intrusion simulation and (c) resampled to the resolution of the magnetization model. This can be thought of as a mask which we place over the preintrusion 3-D magnetization patterns, resulting in postintrusion magnetization patterns, an example of which (with 256 km and 12 km horizontal and vertical coherence wavelengths, respectively) is shown in cross section. (d) Note that positive and negative magnitudes mean magnetization direction at $+45^\circ$ and -45° (see text). (e) The resulting magnetic field magnitude at an altitude of 185 km after the demagnetization of 100 such random magnetization patterns are shown with light gray lines, with mean and standard deviations shown in black.

- the same crust cannot further demagnetize the crust. The derived intrusion volumes may thus be a factor of 2 or more higher and hence are a lower bound.
3. **The dominant magnetic mineral is unknown.** Minerals with higher Curie temperatures can support a magnetized layer to greater depths below the surface. Intrusions below the maximum depth do not affect magnetization. Therefore, in addition to the layer thickness the depth of the magnetized layer is important in terms of the ease with which these intrusions may demagnetize the crust.

substantial spread in the best fit values of intrusion radii and volumes, but the fits are nonetheless instructive. For magnetic field strength to go so close to zero at the centers of the NALF and SALF, a substantial area of extremely weak or zero magnetization must exist. Under the assumption that this area was magnetized with a similar strength and coherence wavelength similarly to its surroundings prior to any postdynamo magmatism, the diameter of each intrusive body must be at least ~ 320 km, most likely around 450 km, and at most 600 km, with the inferred areas of the intrusive bodies beneath the SALF and NALF the same (within error).

5.1. Systematic Uncertainties in Intrusion Volumes

The radii and areas of intrusive bodies are well constrained, and therefore, the estimates of those quantities are robust (Figure 6 and Table 3). However, our estimates of the corresponding total intrusion volumes given in Table 1 and Figure 5 are complicated by the following factors:

1. **Thickness of magnetized layer.** The simulations assumed a 40 km thick magnetized domain prior to intrusion, necessitating intrusion over this depth to fully demagnetize the crust to match observations. However, the preintrusion magnetization could reside in a single layer several times thinner than 40 km and still reasonably explain the magnetic fields measured above the surrounding region. Therefore, the derived intrusion volumes are upper bounds.
2. **Saturation effects.** The simulations show that a crustal replacement ratio of 0.5 is sufficient to fully thermally demagnetize the crust. Subsequent intrusion into

Table 2. Description of the Space of Thermal Demagnetization Model Input Parameters That Were Used to Create the Database of Predicted Radial Magnetic Field Profiles, With Which Measured Profiles Were Compared^a

Parameter	No. of Values	Range of Values
Coherence wavelength	3	256, 512, 1024 km
Magnetization strength	75	0.1–100 A/m (log spaced)
Ratio of intruded magma to preexisting crustal volume	5	0.0007, 0.004, 0.02, 0.1, 0.5
Intrusion radius	7	100, 150, 200, 250, 300, 350, 400 km
Curie temperature	3	325°C, 580°C, 670°C

^aThe table lists the parameters along with the number of discrete values of each parameter that were used and the range of those values. Note that 200 models were run for all combinations of these parameters. Therefore, $3 \times 75 \times 5 \times 7 \times 3 \times 200 = 4,725,000$ model runs.

Even with these systematic uncertainties, we can nonetheless estimate an overall minimum for intrusion volume. The same stochastic magnetization model described in section 4.1 reproduces the observed average regional magnetic field strength of ~ 40 nT with the following four assumptions: (1) a magnetized layer thickness of d km, (2) a magnetization strength of $(20/d)$ A/m, (3) a lateral magnetization coherence wavelength of

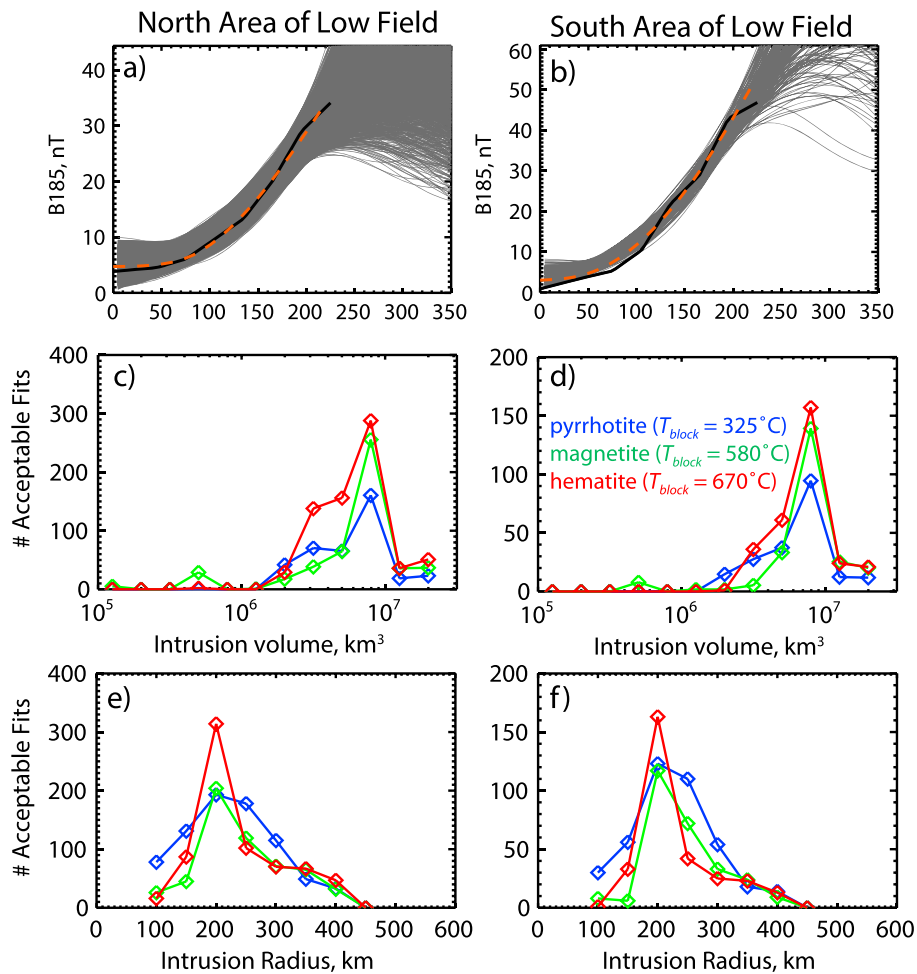


Figure 5. Information concerning fits of thermal demagnetization model results to B_{185} data for both the (a, c, and e) NALF and (b, d, and f) SALF zones. (Figures 5a and 5b) The azimuthally averaged radial profiles of measured B_{185} data (black), compared with all simulated profiles within one sigma of the χ^2 minimum (gray), i.e., the “good” fits. The best individual fit in Figures 5a and 5b is shown as an orange dotted line. Figures 5c and 5d show the number of acceptable fits for each possible value of modeled intrusion volume. Figures 5e and 5f show the number of acceptable fits for each model value of intrusion radius. The blue, green, and red curves represent the models where the magnetic mineral was pyrrhotite, magnetite, and hematite, respectively.

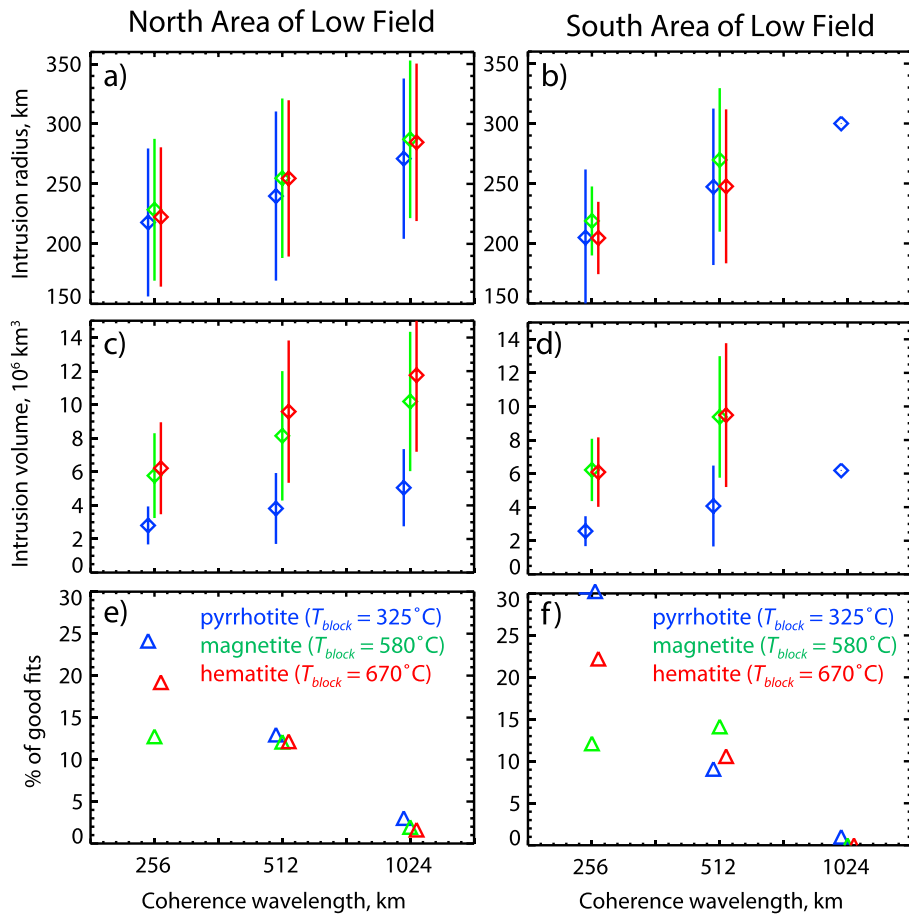


Figure 6. Results of fitting thermal demagnetization model results to B_{185} data for both the (a, c, and e) NALF and (b, d, f) SALF zones. Figures 6a and 6b show the mean and standard deviation of the intrusion radius for each of the good fits shown in Figures 5a and 5b, for each of the three Curie temperatures and coherence wavelengths. Figures 6e and 6f show the volume of intruded material above the Curie isotherm. Figures 6e and 6f show the distribution of the good fits among the Curie temperatures and coherence wavelengths. There is no standard deviation on the radius or intrusion volume for pyrrhotite and 1024 km coherence wavelength because there was only a single successful model.

400 km (chosen on the basis of the goodness of fits shown in Figures 5e and 5f), and (4) no vertical magnetization gradients within the layer. In other words, a high but plausible (based on magnetic mineralogy [e.g., Dunlop and Arkani-Hamed, 2005]) magnetization strength of $\sim 20 \text{ A/m}$ would require a cumulative magnetized depth of $\sim 2 \text{ km}$. In the highly unlikely event that all of an intrusion were concentrated in or very near the same depths as the preintrusion magnetization, all of which was pyrrhotite, we find an absolute minimum intrusion volume of $2.5\text{--}3 \times 10^5 \text{ km}^3$ for each body below the NALF and SALF zones, ~ 10 times lower than the overall best fit intrusion volumes for these regions (shown in the right column of Table 3). However, given the likely stochastic nature of magmatic intrusions, both before and after the cessation of the Martian dynamo, most of the depth to the Curie isotherm was probably intruded by magma. The intrusion estimates in Table 3 are therefore unlikely to be gross overestimates and could in fact be underestimates by a factor of 2 due to the aforementioned saturation effects (i.e., 50% crustal replacement gives the same total demagnetization as 100 or 200%). In summary, these considerations show that, although magnetic field data can robustly be used to determine the radius to which total thermal demagnetization must have occurred via magmatic intrusion, these data provide much looser bounds on intrusion volumes because orbital data can be used to constrain neither the distribution of postdynamo intrusions nor the predynamo distribution of magnetization.

Table 3. Best Fit Results to the Azimuthal Average of Magnetic Field Over the NALF and SALL Zones^a

Magnetic Mineral	Curie Isotherm Depth (km)	% of Good Fits	Intrusion Radius (km)				Intrusion Volume ($\times 10^6 \text{ km}^3$) Shallower Than Curie Isotherm ^b		
			$\lambda_{coh} = 256 \text{ km}$	$\lambda_{coh} = 512 \text{ km}$	$\lambda_{coh} = 1024 \text{ km}$	All λ_{coh}	$\lambda_{coh} = 256 \text{ km}$	$\lambda_{coh} = 512 \text{ km}$	All λ_{coh}
North area of low field (NALF)	Pyrrhotite	19.7	40.1%	218 \pm 62	240 \pm 70	271 \pm 73	228 \pm 67	2.8 \pm 1.1	3.8 \pm 2.1
	Magnetite	35	26.8%	228 \pm 59	255 \pm 67	287 \pm 66	244 \pm 65	5.8 \pm 2.5	8.1 \pm 3.9
	Hematite	40	33.1%	222 \pm 58	255 \pm 65	285 \pm 66	237 \pm 64	6.2 \pm 2.7	9.6 \pm 4.2
All minerals		100%		221 \pm 60	249 \pm 67	279 \pm 66	234 \pm 66	4.6 \pm 2.7	7.1 \pm 4.3
	% of good fits			56.1%	37.2%	6.7%	100%	56.1%	37.2%
	Pyrrhotite	19.7	40.9%	205 \pm 57	247 \pm 65	300	217 \pm 62	2.6 \pm 0.9	4.1 \pm 2.4
South area of low field (SALL)	Magnetite	35	26.3%	219 \pm 29	270 \pm 60	-	246 \pm 54	6.2 \pm 1.9	9.4 \pm 3.6
	Hematite	40	32.8%	205 \pm 30	248 \pm 64	-	218 \pm 48	6.1 \pm 2.1	9.5 \pm 4.3
	All minerals			65.1 %	33.8%	1.1%	225 \pm 57	4.5 \pm 2.4	8.0 \pm 4.3
% of good fits				65.1 %	33.8%	1.1%	100%	65.1 %	33.8%
								1.1%	100%

^aThis is a tabular form of the results shown in Figure 6. Best fit intrusion radii and intrusion volumes are shown for the three magnetic minerals, separately for assumed magnetization coherence wavelengths of 256 km, 512 km, and 1024 km. The percentage of good fits for each coherence wavelength and magnetic mineral is also shown. Overall, best fit results are shown in bold in thick boxes.

^bAdditional systematic uncertainties in intrusion volumes are discussed in section 5.1.

5.2. Influence of Magnetic Curie Temperatures and Coherence Wavelengths of Magnetization

Interestingly, we find no statistically significant difference between the best fit radii of intrusion for each magnetic mineral. We note that this is in contrast to the ~50 km difference among minerals in the location of intrusion boundaries in southwestern Tharsis derived by *Lillis et al.* [2009]. The difference between the two studies is likely due to the following differences in method: (1) the geometry of the inferred intrusion in the former study was different (an extended boundary rather than a cylindrical shape), (2) *Lillis et al.* [2009] used a physically less realistic rectangular checkerboard pattern of magnetization, and (3) single B_{185} profiles were fit to ensemble averages of such profiles from magnetization simulations instead of comparing azimuthal averages of measured data with models, as we do in this study.

Nonetheless, in our simulations a slightly larger fraction of the good fits (~40%) are for models with pyrrhotite (and its lower Curie temperature of 325°C), with smaller fractions (~27% and ~33%) composed of hematite and magnetite, respectively. This preference for pyrrhotite-bearing models may be due to more complete demagnetization in the intrusion zone occurring for lower Curie temperatures, although the effect is not a large one.

We also note a strong preference in model fits for smaller preintrusion magnetization coherence wavelengths of 256 km and 512 km, compared with the approximate global average of 1024 km [*Lillis et al.*, 2010]. For both NALF and SALF, simulations with these wavelengths provide ~60%, ~35%, and ~5% or less of the acceptable fits, respectively. As mentioned in section 3, it may be that the impact demagnetization of the nearby Utopia and (in particular) the Isidis Basins resulted in the formation of a narrow zone of magnetized material, approximately 200–300 km across, to the east of Syrtis. This contribution to the azimuthal average may explain the preference for the smaller coherence wavelengths.

5.3. Constraining Demagnetization Beneath the Caldera

Our modeling described thus far assumed only two centers of intrusion (i.e., one each under the NALF and SALF zones). This choice was guided by the morphology of the magnetic field map as measured at 185 km altitude. As seen in Figure 1, the NALF and SALF modeled intrusion zones overlap with one another around the caldera complex, where the magnetic field magnitude (12–20 nT) is substantially lower (by a factor of 2–3) than to the east or west of the caldera. Because the field over the caldera does not go to zero, one possibility is that substantial magnetization remains beneath the caldera complex. This would be the unambiguous conclusion if the magnetic field data were collected at an altitude considerably lower than the spatial extent of the complex (e.g., 30 km). However, at 185 km altitude, the magnetic field is dominated by contributions from magnetization wavelengths on the order of this altitude or greater; i.e., magnetization ~200 km away could be responsible for the nonnegligible magnetic field measured directly over the caldera. This relationship between altitude, demagnetization radius, and coherence wavelength was examined in detail by *Lillis et al.* [2010, 2013b].

Nonetheless, useful constraints on the nature of the subsurface magnetization beneath the Syrtis caldera can be derived. We used the same magnetization modeling framework described above to calculate magnetic field profiles expected for a range of diameters (0–600 km) and degrees (0%–100%) of demagnetization for 1000 randomly generated initial magnetization distributions with a horizontal coherence wavelength of 256 km (consistent with the best fits in the previous section). We then calculated the ratios of the modeled magnetic field measured inside 0.5 demagnetization radii (i.e., within half of the radius of demagnetization) to those measured between 1.25 and 2 radii and compared these ratios with analogous measured ratios calculated from the map of B_{185} (i.e., Figure 1a), using only pixels within 45°E or 45°W from Meroe Patera (the small white circle near the center of the larger white circle in Figure 1b). This approach resulted in a probability distribution as a function of fractional magnetization (i.e., that magnetization remaining after the intrusion) and diameter of demagnetization (this technique was also used by *Lillis et al.* [2013a]). As shown in Figure 7, there is a trade-off between fractional magnetization and width (in approximately an east-west orientation) of the demagnetized area beneath the Syrtis caldera complex. Within our model framework, then, an intrusion extending for 500 km indicates that the crust was demagnetized by 20%–50%, whereas an intrusion 350 km across corresponds to a crustal demagnetization of 50%–80%. Similarly, these results show that the measured magnetic field strength is also consistent with demagnetization of ~70–100% inside a region beneath the caldera complex of ≤ 300 km width (100% is consistent with the levels of intrusion per square kilometer inferred for NALF and SALF).

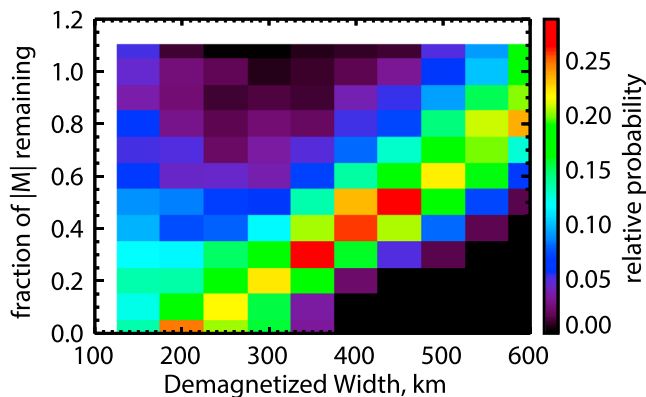


Figure 7. The subcaldera complex demagnetization probability space. Relative probability of occurrence as a function of fractional remaining magnetization is shown for each of 10 values of demagnetized zones of crust whose width ranges from 150 km to 600 km. Thus, for example, a portion of crust beneath the caldera complex crust that is ~40% demagnetized over a width of 500 km fits the data approximately equally well as that which is ~70% demagnetized over a width of 350 km. Note that the largest y axis values are magnetization fractions of 1.1, i.e., 10% higher magnetization than the surroundings.

Using the same model framework described in section 4, we calculate that a completely demagnetized zone 300 km across can be produced by a region of $\geq 50\%$ (by volume) magmatic intrusion that is 150–250 km across (depending on Curie temperature).

In summary, our comparison of model data with measured field intensity data shows that, when considered in isolation from the magnetic fields associated with the NALF and SALF areas, the low but nonzero magnetic field strength over the Syrtis caldera can be explained equally by either (1) complete thermal demagnetization of the upper crust over a narrower intrusive zone (< 250 km) beneath the caldera complex or (2) an intrusive zone comparably as wide as that implied for the SALF and NALF regions (i.e., ~ 500 km) but with approximately half of the intruded volume per unit area, i.e., such that some substantial magnetization remains.

5.4. Intrusion Pattern and Density: Reconciling Gravity and Magnetic Data

The magnetic field data are consistent with two interpretations for the pattern of intrusion, both comparable in size to the Syrtis Major volcanic edifice [Plescia, 2004]. Under one interpretation, there is an approximately “hourglass”- or dog bone-shaped region of total or almost complete thermal demagnetization that extends ~ 1000 km from north to south, and ~ 450 – 500 km from east to west, with the northern and southern extremities separated by a narrower (≤ 300 km wide) neck beneath the caldera complex. The other interpretation is that the intrusive rocks may span the entire elongated 1000 km \times 500 km area, but that directly beneath the caldera complex they have only partially demagnetized the crust.

Gravity data provide additional constraints on the density structure of the crust in the Syrtis Major region, which in turn may shed light on the distribution of relatively dense subsurface intrusive bodies. The large positive free-air gravity anomaly shown in Figure 1d is strongest directly above the caldera and is elongated along the same axes as that of the caldera and the SALF and NALF zones, implying that all three are the result of the same overall pattern of magmatic and volcanic activity. Further, the gravity anomaly is ~ 300 km wide and approximately lenticular in planform, consistent with the “hourglass/dog bone” interpretation of the shape of the region of near-complete thermal demagnetization.

To interpret the significance of this gravity data, we must evaluate the relative importance of density changes from two processes: porosity reduction as intrusions heat the crust [Kiefer, 2013] and the density contrast between frozen intrusions themselves and the surrounding crust.

Because porosity loss depends on viscosity, crustal heating and thickening during episodes of intrusive magmatism may accelerate compaction, thereby influencing local bulk density [Kiefer, 2013]. To assess the potential contribution of compaction to the gravity signature of Syrtis Major, we coupled a simple model of porosity reduction by viscous flow with a one-dimensional model of crustal heating during Syrtis magmatism.

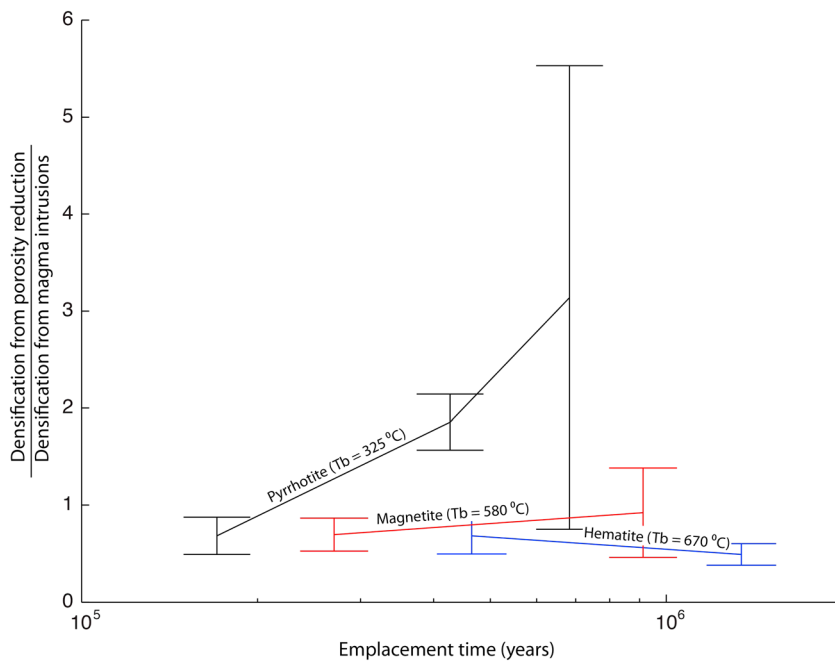


Figure 8. The relative importance of intrusive versus porosity-loss density change as a function of magmatic emplacement time scale (the error bars denote two standard errors from binned mean values). For realistic emplacement time scales ($>10^4$ years), dense intrusions should strongly influence gravity anomaly observations.

Changes in porosity, φ , from viscous flow can be modeled as

$$\frac{d\varphi}{dt} = -\varphi \frac{P}{\mu},$$

where μ is the viscosity and P is the lithostatic pressure [Fowler, 1985]. One-dimensional simulations with stochastic sill emplacement (as opposed to the three-dimensional sill emplacement simulations described in section 4.2) predict the porosity loss associated with several scenarios for Syrtis Major magmatism, assuming an initial porosity profile that decays exponentially with depth [Clifford and Parker, 2005], as well as a power law expression for the temperature-dependent viscosity of dry diabase [Mackwell et al., 1998]. The thermal evolution of the magmas is computed by solving the one-dimensional heat diffusion equation, accounting for latent heat released by crystallization.

We find that the relative importance of densification associated with compaction depends on the magnetic mineralogy (and more weakly on the time scale for emplacement of the intrusions that demagnetize the crust). The Curie temperature of hematite (670°C) is higher than that of magnetite (580°C), which in turn is higher than that of pyrrhotite (325°C). In the presence of a preintrusion geothermal gradient, higher Curie temperatures imply a greater thickness of crust that must be demagnetized (presumably by deep intrusive bodies). However, deeper crust will have minimal initial porosity, and therefore, such deep intrusions will cause negligible compaction. As shown in Figure 8, if the primary magnetic mineral is pyrrhotite, and magmas must intrude only the porous uppermost crust to remove the magnetic remanence, compaction associated with demagnetization could be as important as or more important than the density contrast between the magmas and the country rock. The positive gravity anomaly centered above the caldera complex could then reflect a region of originally porous material that underwent compaction during the crustal heating that accompanied Syrtis Major magmatism.

On the other hand, for magnetic remanence hosted by magnetite or hematite, and for realistic magmatic time scales ($>10^6$ years), the density perturbation from the intrusions themselves is greater than that from compaction (Figure 8). Thus, if either magnetite or hematite is the primary magnetic mineral in the Martian crust, then the gravity data may directly reflect the subsurface structure and composition of the Syrtis Major magmatic system. In this case, we interpret the gravity anomaly as evidence that density contrasts and intrusive concentrations are greatest beneath and directly to the north of the Syrtis Major caldera complex.

5.5. Constraints on Magma Composition

The low magnetic field strength measured above the Syrtis volcanic edifice indicates that a substantial fraction of the upper crust beneath the edifice has been intruded by magma. Likewise, the gravity anomaly data point to a relatively high-density body of material beneath the surface. Intrusion events constrained by these geophysical measurements provide further context for the generation of some of the most diverse igneous compositions on Mars. As briefly mentioned already in section 3.3, lithologies measured spectroscopically in this area range from picritic basalt to rhyolite [Christensen *et al.*, 2005; Hamilton and Christensen, 2005; Mustard *et al.*, 2005]. The most evolved dacitic [Christensen *et al.*, 2005] and rhyolitic [Wray *et al.*, 2013] magma compositions inferred in Nili Patera imply either extensive fractionation of intruded magmas, partial melting of the crust, or a combination of both. Based on the current spectroscopic evidence it is not possible to distinguish between these scenarios. In the case of the most felsic material, data from the Compact Reconnaissance Imaging Spectrometer indicate a feldspar-rich lithology with less than 2% mafic phases. Wray *et al.* [2013] modeled the generation of these silicic magmas through fractional crystallization, which occurred most efficiently when the magma was in a highly crystalline or mush state [Dufek and Bachmann, 2010]. This model predicts a large mafic cumulate body from which the more silicic magmas were extracted, likely in multiple episodes. Such a model is consistent with the geophysical observations of a dense body producing the gravity anomaly and the large amount of mafic intrusions required for the ER magnetic signature at Syrtis. An alternative interpretation of these outcrops is that they are anorthosites with very high calcium pyroxenes [Rogers and Nekvasil, 2015].

5.6. Ratio of Intruded to Erupted Volumes

The total volume of magma erupted onto the surface at Syrtis is $1.6\text{--}3.2 \times 10^5 \text{ km}^3$ [Hiesinger and Head, 2004]. If crustal magnetization existed to depths of the Curie isotherm prior to magmatic activity, then the minimum estimate for intruded magma volume in this depth range at this site ranges from 4 to $19 \times 10^6 \text{ km}^3$, depending on magnetic mineral. These are minima because they result from 50% crustal replacement by intrusion; as stated earlier further intrusion does not cause further demagnetization. Thus, the implied minimum ratio of intruded to extruded volumes of magma (hereafter termed the "I/E ratio") is thus 15–120:1, with an average of ~47:1. As an example, if the magnetic mineral is pyrrhotite and the extruded volume is $3.2 \times 10^5 \text{ km}^3$, then the I/E ratio is at least 15. This is substantially larger than both the global estimate for Mars of 5–12:1 [Greeley and Schneid, 1991] and the mean value for Earth of 10:1 [Crisp, 1984]. Even on Earth, however, the I/E ratio is highly variable and difficult to constrain, varying from <1:1 to >100:1, and there is no clear correlation with tectonic setting [White *et al.*, 2006]. Thus, a direct inference is that these I/E ratios imply that, at least within the Syrtis volcanic and tectonic settings, magmas were less likely to erupt than those on Earth or elsewhere on Mars.

5.7. Implications for the Origin of Syrtis Magmatism

The volume, lateral extent, and duration of magmatic activity at Syrtis provide insight into mantle dynamics and the origin of the volcanic complex. There are three principal explanations for volcanism on Mars: (1) thermal insulation by an insulating crust of the planet's interior leads to pervasive melting in the shallow mantle [e.g., Schumacher and Breuer, 2006, 2007], (2) impacts heat and melt crust and mantle [Reese, 2004], and (3) upwelling in the mantle generates melt by decompression [e.g., Harder, 1998; Kiefer, 2003; van Thienen *et al.*, 2006; Wenzel *et al.*, 2004; Zuber, 2001]. Here we use the inferred volume of magma and its spatial distribution to evaluate these three possibilities in order. Note that these are not mutually exclusive globally or even regionally.

The thermal insulation mechanism [Schumacher and Breuer, 2006, 2007] must play some role in controlling the subsurface thermal state. However, this mechanism works best if the thermal conductivity is at the low end ($\sim 2 \text{ W m}^{-1} \text{ K}^{-1}$) of the range that is likely for Martian crustal rocks. For more likely conductivities, $k > 3 \text{ W m}^{-1} \text{ K}^{-1}$, the insulation mechanism is much less important. Moreover, this mechanism requires thick crust to be effective. The inferred crustal thickness in the Syrtis Major region is 50–60 km, only slightly larger than the global average value [Neumann *et al.*, 2004]. If the thermal insulation mechanism was the dominant process for producing magma in Syrtis, we would expect to find similar large volcanoes in many other areas of the Martian highlands. Because such edifices are in fact relatively rare, some other mechanism must be the dominant magma-producing process in Syrtis.

Large impacts will melt the crust and uppermost mantle and deposit large amounts of heat within the mantle. This latter process, in turn, leads to buoyant upwelling and further (adiabatic decompression) melting. Numerical simulations show that these upwellings persist for only tens of millions of years [Roberts *et al.*, 2009; Roberts and Arkani-Hamed, 2012], whereas volcanism at Syrtis Major continued for a much longer period of time [Robbins *et al.*, 2011].

Under the assumption that magnetization exists at all depths shallower than the mineral-dependent historical Curie isotherm (~20–60 km), complete demagnetization of the crust requires that most of the material above this isotherm is composed of intrusions emplaced after the Martian dynamo ceased. Petrologic modeling using compositions inferred from orbital gamma ray spectrometry suggests that the Syrtis basalts formed at a mantle potential temperature of 1380°C and a melt fraction of about 10% [Baratoux *et al.*, 2011]. Application of this same remote sensing technique to Gusev crater basalts underestimates the potential temperature by >50 K and the melt fraction by about 5% relative to laboratory studies that are constrained by in situ composition measurements by the Spirit rover [Filiberto *et al.*, 2010]. Applying this correction to Baratoux *et al.*'s [2011] Syrtis results, we estimate a mantle potential temperature of at least 1430°C and a melt fraction of about 15% at Syrtis, values that are consistent with a hot, upwelling mantle plume beneath Syrtis.

Two-dimensional [Li and Kiefer, 2007; O'Neill *et al.*, 2007] and three-dimensional [Golabek *et al.*, 2011; Keller and Tackley, 2009] mantle convection simulations show that mantle plumes can subsist on Mars and may provide the best explanations for magmatism at Tharsis and Elysium [Li and Kiefer, 2007]. The lateral extent of melting in the modeled plumes of ~500 km is similar to that of the intrusive complex beneath Syrtis. Although Li and Kiefer [2007] modeled melt production associated with a single plume in spherical axisymmetric geometry, convection simulations in a fully three-dimensional sphere show that multiple plumes can be active at the same time in early Martian history [Harder, 1998; Sekhar and King, 2014], so it is reasonable that Syrtis, Tharsis, and Elysium may have all been volcanically active at the same time. The formation of a volcanic edifice [Pinel, 2003] and overpressure within intruded bodies of magma [Karlstrom *et al.*, 2009] create stresses that focus rising magma toward the volcanic center. However, the tensile strength of basalt and other lithologies that limit overpressure, <10 MPa [Gudmundsson, 2011], is insufficient for rising magma to be drawn laterally by more than a few tens of kilometers toward magma chambers [Karlstrom *et al.*, 2009]. We therefore expect that a region that hosts intruded magma bodies should overlie a corresponding region in the mantle in which melt is generated, although long-distance lateral transport of magmas through dikes may occur [Ernst *et al.*, 2001].

In sum, the lateral dimensions, total volume, and protracted duration of magmatic activity at Syrtis Major are each consistent with upwelling in the mantle underneath the volcanic center. The total volume of erupted and intruded magmas is comparable to the volume of magma erupted in continental flood basalt provinces on Earth ($\sim 10^6 \text{ km}^3$), eruptions that are usually attributed to large upwellings in the mantle [Richards and Griffiths, 1989]. Mantle convection simulations suggest that, as noted in section 3.2, the eruptive history of Syrtis Major spans ~2.2–3.6 Ga [Robbins *et al.*, 2011]. If a single mantle plume engendered all the magmatism at Syrtis, it must therefore have been stable for ~1–2 Ga. Mantle convection simulations do feature long-lived plumes [e.g., Harder and Christensen, 1996]. However, such simulations also suggest that over the past 4.5 Ga, the number of large upwellings in the Martian mantle should decrease with time [Harder and Christensen, 1996; Keller and Tackley, 2009].

5.8. Structural Control of Magma Flow

The thermal demagnetization pattern, the free-air gravity anomaly, and the topography of the Syrtis Major caldera complex are each elongated, with their axes of elongation almost colinear along a line that is approximately north-northwest (Figure 1). The location of the Syrtis caldera complex in the center of the slightly tilted (with respect to local north) hourglass/dog bone-shaped inferred intrusive complex gives clues as to the paths taken by ascending magma to the surface and hence the role of tectonic stresses beneath the volcano. The following conceptual geologic model may explain the magnetic and gravitational patterns observed at Syrtis Major. Magmatic intrusion beneath the NALF and SALF zones might have relied on crustal shearing and weakening due to overpressure from the main Syrtis magma body. If the main magma body were elongated north-northwest (perhaps due to prior-existing crustal structure, as discussed below), overpressure in the system would have generated Coulomb stresses in a dog bone-shaped pattern that

encouraged transform faulting off axis of the main body. Such off-axis transform faults have been observed in recent volcanic events on Earth during and immediately after the ascent of a pressurized dike [Roman and Heron, 2007; Toda et al., 2002]. Within the four ends of the dog bone structure (two branching ends at each end of the axis of the original magma body), faulting would have initiated in two cross-axis ends which effectively shut off the development of faults in the remaining two ends. These two weakened zones, to the north and south of Syrtis, may have become stable transform shear zones before later enabling the ascent and storage of magma at relatively shallow crustal levels.

The presence of intrusions to the north and south of the Syrtis Major free-air gravity anomaly, tangential to Isidis impact basin, instead of intrusions to the east and west (i.e., the north and south trending branches of the dog bone structure were exploited, as opposed to the east and west trending branches), might be explained by regional structures developed by deep-seated deviatoric stresses following the formation of Isidis. Large-impact structures include listric extensional faults circumferential to the crater cavity [Melosh, 1989; Osinski and Pietrazzo, 2012]. These faults are known to act as pathways for magma ascent following large-impact events [Melosh, 1989]. The Syrtis Major edifice is located in a region in which listric extensional faulting likely occurred in association with the formation and modification of the Isidis Basin. Nili and Amenthes Fossae are likely examples of this same process but which were not used as ascension pathways for major episodes of volcanism. As magma ascended through the magnetized crust, existing faults would have been exploited as the easiest pathways to the surface. Faults in older Noachian terrains have also focused younger volcanism across the Tharsis region [Bleacher et al., 2009; Hauber et al., 2009; Richardson et al., 2013]. As the Syrtis Major edifice grew, it would have been topographically unbuttressed to the east, toward the topographically low Isidis Basin floor (Figure 1b), much like the Hawaiian volcanoes on Earth that are buttressed by adjacent, older volcanoes but are unconstrained topographically toward the ocean. This geometry would have favored the development of structurally weak zones parallel to the unbuttressed flank, which in turn would have enabled the intrusion of blade-like dikes and the formation of volcanic rift zones parallel to the boundary with the lower topography [Rubin and Pollard, 1987]. In this way, magma ascent at depth associated with the formation of Syrtis Major may have demagnetized the ancient, underlying crust in an hourglass-shaped pattern offset ~100 km south from the free-air gravity anomaly. As magma ascended, it would have begun to exploit the listric faults of the Isidis Basin, thereby focusing the volcano's growth along the margin of the basin. The unbuttressed nature of the resulting volcanic pile would have enabled the storage of magma within the volcano in an elongated pattern parallel to the lower topography to the east.

6. Conclusions

We have used thermal-magnetic modeling of subsurface demagnetization to fit magnetic field measurements of the Syrtis Major volcanic system on Mars and then to infer the areal extent and volume of a magmatic intrusive system which may exist beneath the volcano. The intrusive to extrusive ratios derived from this analysis range from 15 to 120:1. The data do not reliably distinguish between the candidate magnetic minerals pyrrhotite, magnetite, and hematite but do favor a coherence wavelength of subsurface magnetization of ~250–500 km, i.e., less than half the global average.

Our model best fit results indicate that a dog bone-shaped region of intrusions lies below Syrtis Major. The shapes of the northern and southern ends of this system are consistent with cylindrical intrusions, each ~400–500 km in diameter, with a central portion (i.e., bridging the ends and extending beneath the caldera complex) about 150–250 km in width.

The spatial extent of this region, ~350,000 km², as well as the longevity of volcanism at the Syrtis center, is consistent with a long-lived mantle plume beneath the volcano. Additionally, the north-south elongation of the region, tangential to the nearby Isidis Basin, suggests a possible rift-zone-like origin for Syrtis magma ascent. The extensive mafic crustal intrusions likely associated with this plume account for both the observed ER magnetic field and the dense residue inferred from free-air gravity anomaly data over Syrtis. The petrologic diversity observed at the surface, including some of the most silicic compositions observed so far on Mars, is consistent with fractionation within an extensive intrusive system, limited partial melting of the crust, or both. The dense cumulate residue in the crust implied by the free-air gravity anomaly data is consistent with a fractionation model in which silicic magmas were removed from a crystalline mush.

The processes discussed in this paper, of magmatic intrusion from mantle upwellings and structural control of magma flow within the crust, are applicable not just to Syrtis Major but to other circum-basin volcanic settings on Mars. This is particularly true around the Hellas Basin, where regional tectonic forces and resulting faulting may have played a substantial role in the origins and development of Hadriacus and Tyrrhenus Montes and Amphitrites and Peneus Paterae.

7. Data Access and Acknowledgments

The electron pitch angle distributions used to construct the map of crustal magnetic field magnitude at 185 km altitude (shown in Figure 1) are freely available at the Planetary Data System (<http://pds.nasa.gov/ds-view/pds/viewDataset.jsp?dsid=MGS-M-ER-4-MAP1%2FANGULAR-FLUX-V1.0>). The free-air gravity maps used (e.g., Figure 2) can be accessed freely at <http://pds-geosciences.wustl.edu/missions/mro/gravity.htm>.

Lillis' and Manga's work was supported by NASA MFRP grant NNX09AN18G and NASA MDAP NNX11AI85G. Black's work was supported by the National Science Foundation FESD program, NSF EAR-1135382. Richardson's and Bleacher's work was supported by NASA grant MDAP NNX14AN02G. Kiefer's work at the Lunar and Planetary Institute was supported by NASA Cooperative Agreement NNX08AC28A. Dufek's work was supported by NASA MFRP grant NNX09AN18G.

References

- Acuña, M. H., et al. (1999), Global distribution of crustal magnetization discovered by the Mars Global Surveyor MAG/ER Experiment, *Science*, 284, 790–793, doi:10.1126/science.284.5415.790.
- Arkani-Hamed, J. (2004), Timing of the Martian core dynamo, *J. Geophys. Res.*, 109, E03006, doi:10.1029/2003JE002195.
- Baratoux, D., M. J. Toplis, M. Monnereau, and O. Gasnault (2011), Thermal history of Mars inferred from orbital geochemistry of volcanic provinces, *Nature*, 472(7343), 338–341, doi:10.1038/nature09903.
- Bevington, P. R., and D. K. Robinson (2003), *Data Reduction and Error Analysis for the Physical Sciences*, 3rd ed., xi, 320 pp., McGraw-Hill, Boston.
- Blakely, R. J. (1995), *Potential Theory in Gravity and Magnetic Applications*, xix, 441 pp., Cambridge Univ. Press, Cambridge England, New York.
- Bleacher, J. E., L. S. Glaze, R. Greeley, E. Hauber, S. M. Baloga, S. E. H. Sakimoto, D. A. Williams, and T. D. Glotch (2009), Spatial and alignment analyses for a field of small volcanic vents south of Pavonis Mons and implications for the Tharsis province, Mars, *J. Volcanol. Geotherm. Res.*, 185(1–2), 96–102.
- Carr, M. H. (1974), Tectonism and volcanism of Tharsis region of Mars, *J. Geophys. Res.*, 79(26), 3943–3949, doi:10.1029/JB079i026p03943.
- Christensen, P. R., et al. (2005), Evidence for magmatic evolution and diversity on Mars from infrared observations, *Nature*, 436(7052), 882–882.
- Clifford, S. M., and T. J. Parker (2001), The evolution of the Martian hydrosphere: Implications for the fate of a primordial ocean and the current state of the northern plains, *Icarus*, 154(1), 40–79.
- Crisp, J. A. (1984), Rates of magma emplacement and volcanic output, *J. Volcanol. Geotherm. Res.*, 20(3–4), 177–211, doi:10.1016/0377-0273(84)90039-8.
- Dekkers, M. J. (1989), Magnetic properties of natural pyrrhotite. II High- and low-temperature behaviour of Jrs and TRM as function of grain size, *Phys. Earth Planet. Inter.*, 57, 266–283.
- Dohm, J. M., et al. (2009), Claritas rise, Mars: Pre-Tharsis magmatism?, *J. Volcanol. Geotherm. Res.*, 185(1–2), 139–156, doi:10.1016/j.jvolgeores.2009.03.012.
- Dufek, J., and G. W. Bergantz (2005), Lower crustal magma genesis and preservation: A stochastic framework for the evaluation of basalt-crust interaction, *J. Petrol.*, 46(11), 2167–2195, doi:10.1093/petrology/egi049.
- Dufek, J., and O. Bachmann (2010), Quantum magmatism: Magmatic compositional gaps generated by melt-crystal dynamics, *Geology*, 38(8), 687–690.
- Dunlop, D. J. (2009), Continuous and stepwise thermal demagnetization: Are they equivalent?, *Geophys. J. Int.*, 177(3), 949–957, doi:10.1111/j.1365-246X.2009.04152.x.
- Dunlop, D. J., and J. Arkani-Hamed (2005), Magnetic minerals in the Martian crust, *J. Geophys. Res.*, 110, E12S04, doi:10.1029/2005JE002404.
- Elliot, D. H., T. H. Fleming, P. R. Kyle, and K. A. Foland (1999), Long-distance transport of magmas in the Jurassic Ferrar large igneous province, Antarctica, *Earth Planet. Sci. Lett.*, 167(1–2), 89–104.
- Ernst, R. E., E. B. Grosfils, and D. Mege (2001), Giant dike swarms: Earth, Venus, and Mars, *Annu. Rev. Earth Planet. Sci.*, 29, 489–534.
- Filiberto, J., R. Dasgupta, W. S. Kiefer, and A. H. Treiman (2010), High pressure, near-liquidus phase equilibria of the Home Plate basalt Fastball and melting in the Martian mantle, *Geophys. Res. Lett.*, 37, L13201, doi:10.1029/2010GL043999.
- Fowler, A. C. (1985), A mathematical model of magma transport in the asthenosphere, *Geophys. Astro. Fluid.*, 33, 63–96, doi:10.1080/03091928508245423.
- Glotch, T. D., and A. D. Rogers (2013), Evidence for magma-carbonate interaction beneath Syrtis Major, Mars, *J. Geophys. Res. Planets*, 118, 126–137, doi:10.1029/2012JE004230.
- Golabek, G., T. Keller, T. V. Gerya, G. Zhu, P. J. Tackley, and J. A. D. Connolly (2011), Origin of the Martian dichotomy and Tharsis from a giant impact causing massive magmatism, *Icarus*, 215(1), 346–357, doi:10.1016/j.icarus.2011.06.012.
- Greeley, R., and B. D. Schneid (1991), Magma generation on Mars: Amounts, rates, and comparisons with Earth, Moon, and Venus, *Science*, 254, 996–998.
- Green, T. H. (1972), Crystallization of calc-alkaline andesite under controlled high-pressure hydrous conditions, *Contrib. Mineral. Petrol.*, 34(2), 150–166.
- Green, T. H. (1982), Anatexis of mafic crust and high pressure crystallization of andesite, in *Andesites: Orogenic Andesites and Related Rocks*, edited by R. S. Thorpe, pp. 465–487, John Wiley, Chichester, U. K.
- Green, T. H., and A. E. Ringwood (1968), Crystallization of basalt and andesite under high pressure hydrous conditions, *Earth Planet. Sci. Lett.*, 3(5), 481–489.

- Gudmundsson, S., H. Bjornsson, E. Magnusson, E. Berthier, F. Palsson, M. T. Gudmundsson, T. Hognadottir, and J. Dall (2011), Response of Eyjafjallajokull, Torfajokull and Tindfjallajokull ice caps in Iceland to regional warming, deduced by remote sensing, *Polar Res.*, **30**.
- Hamilton, V. E., and P. R. Christensen (2005), Evidence for extensive, olivine-rich bedrock on Mars, *Geology*, **33**(6), 433–436.
- Harder, H. (1998), Phase transitions and the three-dimensional planform of thermal convection in the Martian mantle, *J. Geophys. Res.*, **103**(E7), 16,775–16,797, doi:10.1029/98JE01543.
- Harder, H., and U. R. Christensen (1996), A one-plume model of Martian mantle convection, *Nature*, **380**(6574), 507–509, doi:10.1038/380507a0.
- Hauber, E., J. Bleacher, K. Gwinner, D. Williams, and R. Greeley (2009), The topography and morphology of low shields and associated landforms of planes volcanism in the Tharsis region of Mars, *J. Volcanol. Geotherm. Res.*, **185**(1–2), 69–95.
- Hauck, S. A., and R. J. Phillips (2002), Thermal and crustal evolution of Mars, *J. Geophys. Res.*, **107**(E7), 5052, doi:10.1029/2001JE001801.
- Hiesinger, H., and J. W. Head (2004), The Syrtis Major volcanic province, Mars: Synthesis from Mars Global Surveyor data, *J. Geophys. Res.*, **109**, E01004, doi:10.1029/2003JE002143.
- Johnson, C. L., and R. J. Phillips (2005), Evolution of the Tharsis region of Mars: Insights from magnetic field observations, *Earth Planet. Sci. Lett.*, **230**(3–4), 241–254, doi:10.1016/j.epsl.2004.10.038.
- Karlstrom, L., J. Dufek, and M. Manga (2009), Organization of volcanic plumbing through magmatic lensing by magma chambers and volcanic loads, *J. Geophys. Res.*, **114**, B10304, doi:10.1029/2009JB006339.
- Keller, T., and P. J. Tackley (2009), Toward self-consistent modeling of the Martian dichotomy: The influence of one-ridge convection on crustal thickness distribution, *Icarus*, **202**(2), 429–443, doi:10.1016/j.icarus.2009.03.029.
- Kiefer, W. S. (2003), Melting in the Martian mantle: Shergottite formation and implications for present-day mantle convection on Mars, *Meteoritics Planet. Sci.*, **38**(12), 1815–1832.
- Kiefer, W. S. (2004), Gravity evidence for an extinct magma chamber beneath Syrtis Major, Mars: A look at the magmatic plumbing system, *Earth Planet. Sci. Lett.*, **222**(2), 349–361, doi:10.1016/j.epsl.2004.03.009.
- Kiefer, W. S. (2013), Gravity constraints on the subsurface structure of the Marius Hills: The magmatic plumbing of the largest lunar volcanic dome complex, *J. Geophys. Res. Planets*, **118**, 733–745, doi:10.1029/2012JE004111.
- Konopliv, A. S., S. W. Asmar, W. M. Folkner, Ö. Karatekin, D. C. Nunes, S. E. Smrekar, C. F. Yoder, and M. T. Zuber (2011), Mars high resolution gravity fields from MRO, Mars seasonal gravity, and other dynamical parameters, *Icarus*, **211**(1), 401–428, doi:10.1016/j.icarus.2010.10.004.
- Li, Q., and W. S. Kiefer (2007), Mantle convection and magma production on present-day Mars: Effects of temperature-dependent rheology, *Geophys. Res. Lett.*, **34**, L16203, doi:10.1029/2007GL030544.
- Lillis, R. J., M. Manga, D. L. Mitchell, R. P. Lin, and M. H. Acuna (2006), Unusual magnetic signature of the Hadriaca Patera volcano: Implications for early Mars, *Geophys. Res. Lett.*, **33**, L03202, doi:10.1029/2005GL024905.
- Lillis, R. J., H. V. Frey, and M. Manga (2008a), Rapid decrease in Martian crustal magnetization in the Noachian era: Implications for the dynamo and climate of early Mars, *Geophys. Res. Lett.*, **35**, L14203, doi:10.1029/2008GL034338.
- Lillis, R. J., H. V. Frey, M. Manga, D. L. Mitchell, R. P. Lin, M. H. Acuna, and S. W. Bouger (2008b), An improved crustal magnetic field map of Mars from electron reflectometry: Highland volcano magmatic history and the end of the Martian dynamo, *Icarus*, **194**(2), 575–596, doi:10.1016/j.icarus.2007.09.032.
- Lillis, R. J., J. Dufek, J. E. Bleacher, and M. Manga (2009), Demagnetization of crust by magmatic intrusion near the Arsia Mons volcano: Magnetic and thermal implications for the development of the Tharsis province, Mars, *J. Volcanol. Geotherm. Res.*, **185**(1–2), 123–138, doi:10.1016/j.volgeores.2008.12.007.
- Lillis, R. J., M. E. Purucker, J. S. Halekas, K. L. Louzada, S. T. Stewart-Mukhopadhyay, M. Manga, and H. V. Frey (2010), Study of impact demagnetization at Mars using Monte Carlo modeling and multiple altitude data, *J. Geophys. Res.*, **115**, E07007, doi:10.1029/2009JE003556.
- Lillis, R. J., S. Robbins, M. Manga, J. S. Halekas, and H. V. Frey (2013a), Time history of the Martian dynamo from crater magnetic field analysis, *J. Geophys. Res. Planets*, **118**, 1488–1511, doi:10.1002/Jgre.20105.
- Lillis, R. J., S. T. Stewart, and M. Manga (2013b), Demagnetization by basin-forming impacts on early Mars: Contributions from shock, heat, and excavation, *J. Geophys. Res. Planets*, **118**, 1045–1062, doi:10.1002/jgre.20085.
- Macke, R. J., D. T. Britt, and G. C. Consolmagno (2011), Density, porosity, and magnetic susceptibility of achondritic meteorites, *Meteoritics Planet. Sci.*, **46**(2), 311–326.
- Mackwell, S. J., M. E. Zimmerman, and D. L. Kohlstedt (1998), High-temperature deformation of dry diabase with application to tectonics on Venus, *J. Geophys. Res.*, **103**(B1), 975–984.
- Melosh, H. J. (1989), *Impact Cratering: A Geologic Process*, 245 pp., Oxford Univ. Press, New York.
- Milbury, C., and G. Schubert (2010), Search for the global signature of the Martian dynamo, *J. Geophys. Res.*, **115**, E10010, doi:10.1029/2010JE003617.
- Milbury, C., G. Schubert, C. A. Raymond, S. E. Smrekar, and B. Langlais (2012), The history of Mars' dynamo as revealed by modeling magnetic anomalies near Tyrhenus Mons and Syrtis Major, *J. Geophys. Res.*, **117**, E10007, doi:10.1029/2012JE004099.
- Morschhauser, A., M. Grott, and D. Breuer (2011), Crustal recycling, mantle dehydration, and the thermal evolution of Mars, *Icarus*, **212**(2), 541–558.
- Mustard, J. F., F. Poulet, A. Gendrin, J. P. Bibring, Y. Langevin, B. Gondet, N. Mangold, G. Bellucci, and F. Altieri (2005), Olivine and pyroxene, diversity in the crust of Mars, *Science*, **307**(5715), 1594–1597.
- Neumann, G. A., M. T. Zuber, M. A. Wieczorek, P. J. McGovern, F. G. Lemoine, and D. E. Smith (2004), Crustal structure of Mars from gravity and topography, *J. Geophys. Res.*, **109**, E08002, doi:10.1029/2004JE002262.
- O'Neill, C. A., A. Lenardic, A. M. Jellinek, and W. S. Kiefer (2007), Melt propagation and volcanism in mantle convection simulations, with applications for Martian volcanic and atmospheric evolution, *J. Geophys. Res.*, **112**, E07003, doi:10.1029/2006JE002799.
- Osinski, G. R., and E. Pietrazzo (2012), *Impact Cratering: Products and Processes*, Wiley-Blackwell, Chichester.
- Özdemir, Ö. (2005), Thermoremanent magnetization of multidomain hematite, *J. Geophys. Res.*, **110**, B09104, doi:10.1029/2005JB003820.
- Pauthenet, R., and L. Bochirol (1951), Aimantation spontanée des ferrites, *J. Phys. Radium*, **12**(3), 249–251, doi:10.1051/jphysrad:01951001203024900.
- Petcovic, H. L., and J. D. Dufek (2005), Modeling magma flow and cooling in dikes: Implications for emplacement of Columbia River flood basalts, *J. Geophys. Res.*, **110**, B10201, doi:10.1029/2004JB003432.
- Pinel, V. (2003), Magma chamber behavior beneath a volcanic edifice, *J. Geophys. Res.*, **108**(B2), 2072, doi:10.1029/2002JB001751.
- Plescia, J. B. (2004), Morphometric properties of Martian volcanoes, *J. Geophys. Res.*, **109**, E03003, doi:10.1029/2002JE002031.
- Rampey, M., and R. Harvey (2012), Mars Hesperian magmatism as revealed by Syrtis Major and the Circum-Hellas volcanic province, *Earth Moon Planets*, **109**(1–4), 61–75, doi:10.1007/s11038-012-9404-0.

- Reese, C. C. (2004), Magmatic evolution of impact-induced Martian mantle plumes and the origin of Tharsis, *J. Geophys. Res.*, 109, E08009, doi:10.1029/2003JE002222.
- Richards, M. A., and R. W. Griffiths (1989), Thermal Entrainment by Deflected Mantle Plumes, *Nature*, 342(6252), 900–902.
- Richardson, J., J. E. Bleacher, and L. Glaze (2013), The volcanic history of Syria Planum, Mars, *J. Volcanol. Geotherm. Res.*, 252, 1–13.
- Roberts, J. H., and J. Arkani-Hamed (2012), Impact-induced mantle dynamics on Mars, *Icarus*, 218(1), 278–289.
- Roberts, J. H., R. J. Lillis, and M. Manga (2009), Giant impacts on early Mars and the cessation of the Martian dynamo, *J. Geophys. Res.*, 114, E04009, doi:10.1029/2008JE003287.
- Robbins, S. J., G. Di Achille, and B. M. Hynek (2011), The volcanic history of Mars: High-resolution crater-based studies of the calderas of 20 volcanoes, *Icarus*, 211(2), 1179–1203, doi:10.1016/j.icarus.2010.11.012.
- Rogers, A. D., and H. Nekvasil (2015), Feldspathic rocks on Mars: Compositional constraints from infrared spectroscopy and possible formation mechanisms, *Geophys. Res. Lett.*, 42, 2619–2626, doi:10.1002/2015GL063501.
- Roman, D. C., and P. Heron (2007), Effect of regional tectonic setting on local fault response to episodes of volcanic activity, *Geophys. Res. Lett.*, 34, L13310, doi:10.1029/2007GL030222.
- Rubin, A. M., and D. D. Pollard (1987), Volcanism in Hawaii, *U.S. Geol. Surv. Prof. Pap.*, 1350(1), 209.
- Schaber, G. G. (1982), Syrtis Major: A low-relief volcanic shield, *J. Geophys. Res.*, 87(B12), 9852–9866, doi:10.1029/JB087ib12p09852.
- Schilling, G. (2011), *Atlas of Astronomical Discoveries*, 243 pp., Springer, New York.
- Schmidt, P. W., and D. A. Clark (1985), Step-wise and continuous thermal demagnetization and theories of thermoremanence, *Geophys. J. R. Astron. Soc.*, 83(3), 731–751, doi:10.1111/j.1365-246X.1985.tb04335.x.
- Schumacher, S., and D. Breuer (2006), Influence of a variable thermal conductivity on the thermochemical evolution of Mars, *J. Geophys. Res.*, 111, E02006, doi:10.1029/2005JE002429.
- Schumacher, S., and D. Breuer (2007), An alternative mechanism for recent volcanism on Mars, *Geophys. Res. Lett.*, 34, L14202, doi:10.1029/2007GL030083.
- Sekhar, P., and S. D. King (2014), 3D spherical models of Martian mantle convection constrained by melting history, *Earth Planet. Sci. Lett.*, 388, 27–37, doi:10.1016/j.epsl.2013.11.047.
- Smith, D. E., et al. (2001), Mars Orbiter Laser Altimeter: Experiment summary after the first year of global mapping of Mars, *J. Geophys. Res.*, 106(E10), 23,689–23,722, doi:10.1029/2000JE001364.
- Tanaka, K. L. (1986), The stratigraphy of Mars, *J. Geophys. Res.*, 91(B13), E139–E158, doi:10.1029/JB091b13p0e139.
- Toda, S., R. S. Stein, and T. Sagiya (2002), Evidence from the AD 2000 Izu Islands earthquake swarm that stressing rate governs seismicity, *Nature*, 419(6902), 58–61.
- van Thienen, P., A. Rivoldini, T. Van Hoolst, and P. Lognonné (2006), A top-down origin for Martian mantle plumes, *Icarus*, 185(1), 197–210, doi:10.1016/j.icarus.2006.06.008.
- Voorhies, C. V. (2008), Thickness of the magnetic crust of Mars, *J. Geophys. Res.*, 113, E04004, doi:10.1029/2007JE002928.
- Wenzel, M. J., M. Manga, and A. M. Jellinek (2004), Tharsis: A consequence of Mars' dichotomy and layered mantle, *Geophys. Res. Lett.*, 31, L04702, doi:10.1029/2003GL019306.
- Werner, S. C. (2009), The global Martian volcanic evolutionary history, *Icarus*, 207(1), 44–68, doi:10.1016/j.icarus.2008.12.019.
- White, S. M., J. A. Crisp, and F. J. Spera (2006), Long-term volumetric eruption rates and magma budgets, *Geochem. Geophys. Geosyst.*, 7, Q03010, doi:10.1029/2005GC001002.
- Williams, J.-P., and F. Nimmo (2004), Thermal evolution of the Martian core: Implications for an early dynamo, *Geology*, 32(2), 97, doi:10.1130/G19975.1.
- Wise, D. U., M. P. Golombek, and G. E. McGill (1979), Tharsis province of Mars: Geologic sequence, geometry, and a deformation mechanism, *Icarus*, 38(3), 456–472, doi:10.1016/0019-1035(79)90200-8.
- Wray, J. J., S. T. Hansen, J. Dufek, G. A. Swayze, S. L. Murchie, F. P. Seelos, J. R. Skok, R. P. Irwin, and M. S. Ghiorso (2013), Prolonged magmatic activity on Mars inferred from the detection of felsic rocks, *Nat. Geosci.*, 6(12), 1013–1017.
- Zuber, M. T. (2001), The crust and mantle of Mars, *Nature*, 412, 220–227, doi:10.1038/35084163.